photonics

MDPI

Article

Design of High-Speed MUTC-PD Under High Input Optical Power Utilizing Combined Analytical and Numerical Methods

Xiyue Zhang and Xiaofeng Duan *

State Key Laboratory of Information Photonics and Optical Communications, School of Electrical and Electronic Engineering, Beijing University of Posts and Telecommunications, Beijing 100876, China; echozhang@bupt.edu.cn
* Correspondence: xfduan@bupt.edu.cn

Abstract

High-speed photodetectors with extended dynamic ranges are critical for emerging optical systems like LiDAR. This paper presents a design methodology for a modified uni-traveling-carrier photodetector (MUTC-PD) that integrates a physics-based analytical model with numerical simulations. The existing analytical models for MUTC-PDs rely on approximations that may not hold under high injection levels and high frequencies, leading to discrepancies between theoretical predictions and practical observations. To address this limitation, we re-examine the governing equations and derive a corrected frequency response analytical model based on drift–diffusion theory by decomposing the device into distinct transport regions, enabling a physically meaningful optimization of the epitaxial layer structure to maximize theoretical intrinsic bandwidth. The calculated results closely match the simulated bandwidth (maximum error less than 6%), demonstrating consistent peak positions and trends. Subsequently, numerical simulations reveal the dynamic evolution of the device's bandwidth under varying incident optical intensities. The results demonstrate that the intrinsic bandwidth initially increases to a peak of 325.82 GHz at 7×10^4 W/cm^2 under -3.5 V, attributed to the drift-enhancement effect driven by the self-induced quasielectric field. Beyond this optimal regime, the space charge effect causes internal field collapse and significant bandwidth degradation. This study establishes bandwidth maintenance capability under high injection as a key metric for linearity, offering a transparent theoretical and practical framework for designing a high-speed MUTC-PD.

Keywords: modified uni-traveling-carrier photodetector; frequency response; high linearity; analytical model

1. Introduction

The rapid development of applications such as LiDAR, free-space optical communication, high-power fiber sensing and advanced optoelectronic test systems has created an urgent demand for faster photodetectors [1–3]. Simultaneously, the performance of photodetectors under high incident optical intensity has become a critical bottleneck for system reliability and dynamic range. The response speed directly determines the upper limits of system performance in terms of ranging accuracy, maximum detection distance and interference immunity. Meanwhile, the maximum incident optical intensity a photodetector can handle defines the upper bound of its linear operating range.

Conventional vertically illuminated p-i-n photodetectors (PIN-PDs) are widely used due to their simple structure and high responsivity [4]. However, the difference between the saturation drift velocities of electrons and holes becomes the primary factor limiting

Check for updates

Received: 26 February 2026
Revised: 31 March 2026
Accepted: 10 April 2026
Published: 13 April 2026

Copyright: © 2026 by the authors. Licensee MDPI, Basel, Switzerland. This article is an open access article distributed under the terms and conditions of the Creative Commons Attribution (CC BY) license.

high-speed performance [5,6]. Under high optical intensity, the slower transit time of photogenerated holes induces a severe space charge effect, leading to internal electric field collapse and rapid photocurrent saturation. High-speed performance of a PIN-PD is restricted by its inherent structure under intense illumination. To address this challenge, a dual-depletion-region photodetector (DDR-PD) was developed by inserting an intrinsic InP layer between the absorption layer and the n-contact based on the PIN-PD, which mitigates carrier accumulation and reduce capacitance, thereby enhancing bandwidth [7,8]. However, the velocity mismatch between carriers remains unresolved and continues to limit saturation performance. In 1997, the uni-traveling-carrier photodetector (UTC-PD) was developed by separating the intrinsic absorber into a heavily p-doped absorber and a lightly n-doped collector [9]. In UTC-PDs, electrons with high mobility serve as the sole carriers traveling towards the collector while holes quickly relax within the absorber, significantly improving response speed.

Despite these advances, existing photodetectors still exhibit limitations when handling incident optical power ranging from milliwatts to watts [10]. High-intensity illumination can not only constrains dynamic range but also induce nonlinear distortion, bandwidth compression, or even permanent damage. Consequently, designing photodetectors that achieve high linearity and high response speed simultaneously has become a core challenge in developing high-performance optical receivers. Modified uni-traveling-carrier photodetectors (MUTC-PDs) demonstrate promising potential [11] to address this challenge. By inserting a depleted absorption layer between the absorber and collector of a UTC-PD, the carrier transport mechanism for electrons in part of the absorber shifts from diffusion to drift. Carrier transit time is reduced within the device, further enhancing transport bandwidth and effectively alleviating the space charge effect. Currently, the performance optimization of MUTC-PDs is comprehensively driven by advancements in epitaxial materials, structural configurations, and advanced fabrication processes [12–22]. An MUTC-PD structure has been reported to achieve a transport bandwidth of 137 GHz with optimized electron transit dynamics under -5 V bias voltage and an incident optical power density of 6×10^4 W/cm^2 [12]. Furthermore, a modified UTC-PD incorporating precise internal electric field regulation has been demonstrated to exhibit an ultra-high 3 dB bandwidth of 206 GHz alongside an external responsivity of 0.81 A/W [13]. Moreover, through the architectural optimization of the cliff layer, a remarkable transport bandwidth approaching 600 GHz under a -2 V bias voltage and 10 mA photocurrent has been reported [14]. However, the internal physical mechanism of an MUTC-PD under high incident optical intensity is complex to analyze, making it difficult to accurately predict its frequency response and high-power behavior using empirical formulas alone. Moreover, while various theoretical approaches have been explored to accurately predict its frequency response and high-power behavior [23,24], immense computational complexity makes them highly inefficient for continuous, multi-parameter structural optimization. Therefore, developing a highly efficient design methodology that combines explicit, physics-based analytical models with numerical TCAD simulations is urgently required to bridge the gap between fundamental transport mechanisms and precise structural optimization of high-performance MUTC-PDs.

In this work, we propose an integrated design approach combining analytical modeling and numerical simulation. Starting from fundamental device physics, a drift–diffusion-based analytical frequency response model is established incorporating carrier continuity and Poisson's equations, enabling precise structural optimization. With the thickness of the total device, absorber and depletion fixed, the thickness of the depleted absorber is adjusted, thereby co-optimizing the thicknesses of the undepleted/depleted absorber and collector to obtain the optimal layer structure configuration. We then employ a commercial simulator

to investigate device performance under high incident optical intensities. The stability of the internal electric field and the maintenance of intrinsic bandwidth are investigated as key physical indicators for the device's linear operation under high optical injection. The results reveal that the intrinsic bandwidth initially increases with optical intensity, peaking at 325.82 GHz at 7×10^4 W/cm^2 under -3.5 V before decreasing due to carrier accumulation-induced space charge effects. This comprehensive methodology overcomes the limitations of a purely empirical formula and provides a transparent theoretical and practical framework for designing a high-speed, high-linearity MUTC-PD.

2. Design Consideration

2.1. Layer Structure of PDs

Figure 1a–d show the band diagrams of several detectors mentioned before. The fundamental operating principle of photodetectors is based on the photoelectric effect in a PN junction. To mitigate the space charge effect induced by slow hole transport, enhanced structures such as the DDR-PD and UTC-PD have been developed based on the conventional PIN-PD. The hole transit distance is reduced by splitting the intrinsic absorption layer of the PIN-PD into an InGaAs absorption layer and an InP collection layer in the DDR-PD, which shortens the carrier transit time while minimally affecting the junction capacitance (the relative permittivities of InGaAs and InP are similar), thereby enhancing high-speed performance. The UTC-PD further improves response speed by replacing the intrinsic absorber with a heavily p-doped layer, enabling high-mobility electrons to serve as the only active transport carriers and effectively suppressing the detrimental impact of sluggish hole transport. However, a simple UTC-PD structure may be not the optimal candidate to obtain the optimum photoresponse under the premise of ensuring responsivity, since the transit time of electrons is proportional to the square of the thickness of the active region [25]. The MUTC-PD addresses this limitation by making the absorber partially depleted, thereby converting a portion of the electron transport from diffusion to drift, significantly alleviating electron accumulation at the interface and simultaneously reducing the device junction capacitance. As a result, the MUTC-PD achieves synergistic improvements in both intrinsic bandwidth and RC-limited bandwidth.

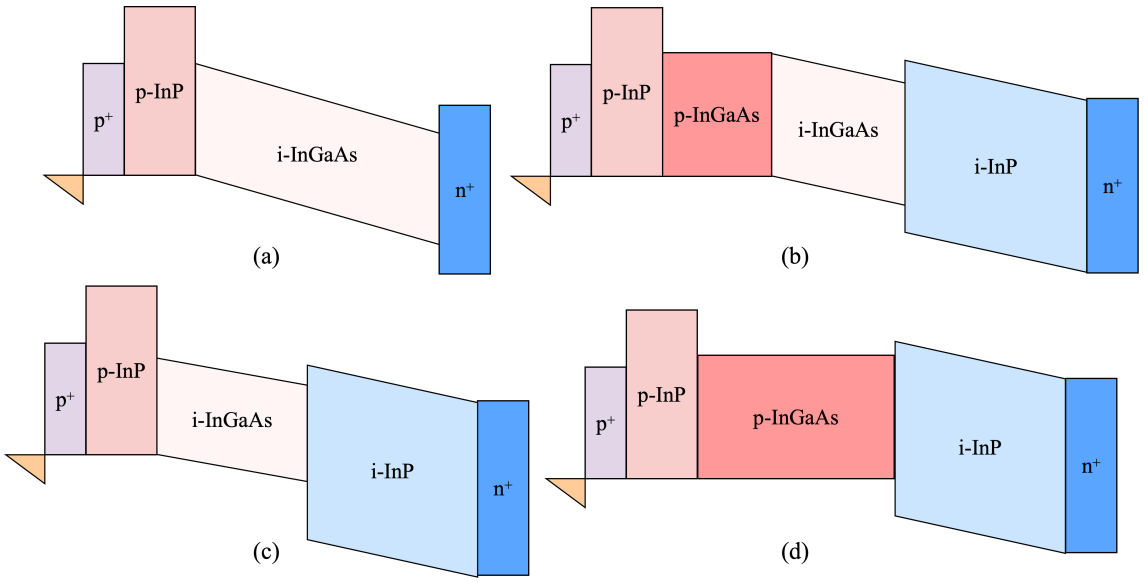


Figure 1. Schematic energy band diagrams of photodetectors: (**a**) PIN-PD, (**b**) DDR-PD, (**c**) UTC-PD and (**d**) MUTC-PD.

Figure 2 provides a qualitative comparison of four photodetectors' features with the same thickness and area of the active region. In the latter three structures, the absorption layer thickness equals the collection layer thickness. For vertically illuminated photodetectors operating without internal avalanche gain and assuming an ideal anti-reflection coating, the expression for responsivity can be written as follows [26]:

$$R = \frac{q}{hf}(1 - e^{-\alpha W_{ab}}) \quad (1)$$

where α represents the optical absorption coefficient, and W_{ab} denotes the thickness of the active region. It is evident that the responsivity of a photodetector fundamentally depends on the material and thickness of the active region. Therefore, all four devices exhibit consistent responsivity. Considering the difference in depletion thickness of the four structures, the MUTC-PD delivers superior performance in terms of both transient response and linearity, while maintaining relatively low capacitance and minimal space charge effect. These advantages highlight its strong potential for applications in high-speed optical communication systems.

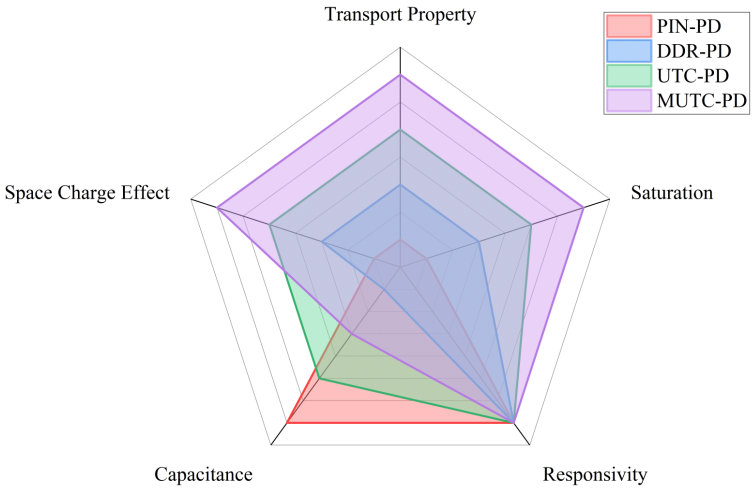


Figure 2. Feature comparison of four PD structures with the same area and thickness of the active region (four points coincide for responsivity). The chart provides a qualitative comparison of the relative performance trade-offs among the four structures.

2.2. Trade-Off

Bandwidth and responsivity are the primary performance metrics for device application in current optical communication systems. However, in applications involving intense illumination, the saturation output characteristics become equally critical and are intrinsically coupled to the bandwidth. Among the underlying physical mechanisms, the space charge effect—a nonlinear phenomenon—serves as the primary limitation on saturation behavior which arises from the accumulation of photogenerated carriers under intense illumination and the velocity saturation of drifting carriers. Both the type of dominant carrier and the electric field distribution within the device are key determinants of such nonlinearities. From a fundamental operational perspective, the MUTC-PD employs electrons as the sole active transport carriers, thereby inherently alleviating the carrier pile-up caused by the low mobility of holes. Meanwhile, the externally applied reverse bias voltage is the principal external parameter for adjusting the internal electric field profile. On the one hand, increasing the reverse bias enhances the degree of the depleted region, delaying the onset of the nonlinear space charge effect. On the other hand, under an appropriate bias condition, electrons can be swept out of the high-field region at overshoot velocity, significantly suppressing charge screening induced by carrier accumulation. Synergistically

taking these intrinsic and extrinsic factors into account, the MUTC-PD achieves the lowest space charge effect among mainstream photodetectors under identical junction areas and reverse bias conditions, enabling it to deliver simultaneously excellent high-power linearity and broadband frequency response.

2.3. Analytical Calculation of MUTC-PD's Photoresponse

Figure 3 illustrates the energy band diagram of the MUTC-PD, alongside the current density components utilized for frequency response calculation. While the MUTC-PD shares a similar heterostructure with the conventional UTC-PD, it incorporates an additional undoped absorption layer—analogous to that of a PIN-PD—to simultaneously enhance responsivity and transit-time-limited bandwidth. The response of the photodetector is derived based on a drift–diffusion model centered on the 1D carrier continuity equation and Poisson's equation. Based on the analysis mentioned before, the analytical model for the AC small-signal frequency response of the MUTC-PD is established using a theoretical framework analogous to that of PIN-PDs and UTC-PDs. However, this derivation necessitates the implementation of new boundary conditions at W_A and W_B, along with corresponding modifications to the equations. The detailed analytical procedure is presented as follows.

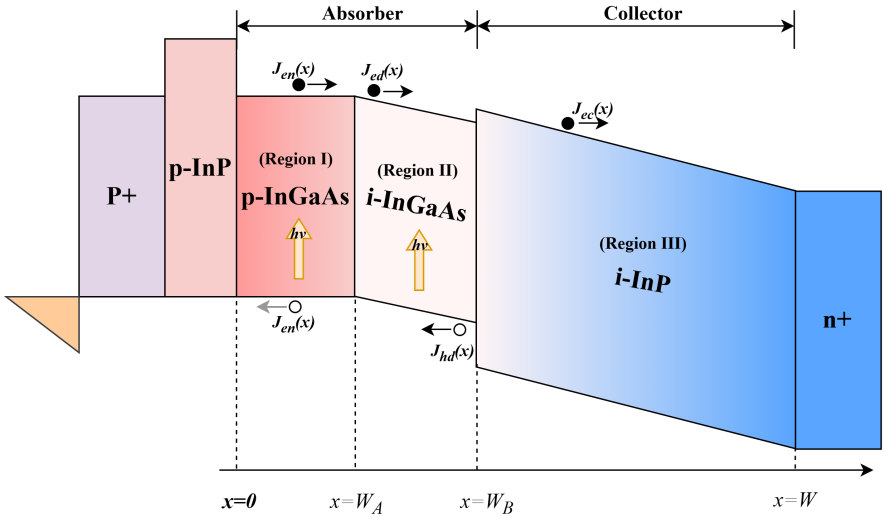


Figure 3. Analytical model schematic of the MUTC-PD used for small-signal carrier transport analysis.

The device structure is divided into three distinct regions along the transport direction x: the p-type absorption layer (Region I, $0 \le x \le W_A$), the undoped absorption layer (Region II, $W_A \le x \le W_B$), and the undoped collection layer (Region III, $W_B \le x \le W$), where W represents the total active layer thickness. The general expression for the total photocurrent density is given by [27]

$$J_{tot} = \frac{1}{W}\int_0^W \left(J_e + J_h + \varepsilon \frac{\partial E}{\partial t} \right) dx \tag{2}$$

where J_e (J_h) denotes the electron (hole) current density, ε is the permittivity, and E is the electric field within the depletion region. Under short-circuit conditions, the integral of the displacement current term (associated with $\partial E/\partial t$) over the device length vanishes. Based on the distinct origins of carrier generation, the total photocurrent can be decomposed into three components: the diffusion current in the p-type highly doped absorber, the drift current in the depleted absorber, and the electron drift current in the collection layer. Consequently, Equation (2) can be reformulated as

$$J_{tot}(\omega) = \frac{1}{W}\left[\int_0^{W_A}(J_{en}+J_{hn})\,dx + \int_{W_A}^{W_B}(J_{ed}+J_{hd})\,dx + \int_{W_B}^{W} J_{ec}\,dx\right] \tag{3}$$

Here, $J_{en}(J_{hn})$ and $J_{ed}(J_{hd})$ denote the electron (hole) current densities in the non-depleted and depleted absorber, respectively, while J_{ec} represents the electron current density component in the collection layer. Consequently, the first and second terms correspond to the optical response generated in the p-type doped absorber and the depleted absorber under optical excitation, whereas the third term represents the response in the collection layer where no photogeneration occurs. The current densities J_e and J_h are derived by solving the carrier continuity equations. The specific expressions for the respective regions are formulated as follows [26]:

$$\frac{\partial n}{\partial t} = G - \frac{n}{\tau} + D_e\frac{\partial^2 n}{\partial x^2}, \qquad (0 \le x \le W_A) \tag{4a}$$

$$\frac{\partial p}{\partial t} = G - \frac{p}{\tau} - \frac{\partial}{\partial x}\{\mu_h(N_a+p)E\}, \qquad (0 \le x \le W_A) \tag{4b}$$

$$\frac{\partial n}{\partial t} = G - \frac{n}{\tau} + \frac{\partial}{\partial x}(nv_e), \qquad (W_A \le x \le W_B) \tag{4c}$$

$$\frac{\partial p}{\partial t} = G - \frac{p}{\tau} - \frac{\partial}{\partial x}(pv_h), \qquad (W_A \le x \le W_B) \tag{4d}$$

where n (p), v_e (v_h), μ_h, D_e, G, τ, N_a and E represent the photogenerated electron concentration (hole), electron saturation velocity (hole), hole mobility, electron diffusion coefficient, carrier generation rate, carrier recombination lifetime, p-type doping concentration, and electric field acting on the carriers, respectively. G is typically expressed in the form $G(x) = G(0)\exp(-\alpha x)$, where G_0 is the surface generation rate and α is the absorption coefficient. Solving the aforementioned equations yields the carrier concentrations within the p-type absorber, depleted absorber, and collection layer. In the p-type absorber, the hole concentration is approximated by the doping concentration. Furthermore, it is assumed that both electrons and holes travel at their saturation velocities within the undoped depletion region. Subsequently, the spatial dependence of each current density component with respect to position x is analyzed as follows.

In Region I, electron transport is governed by the diffusion–drift equation, while holes undergo rapid relaxation within the dielectric relaxation time, the same as the carrier transport mechanism of a conventional UTC-PD. However, due to the injection of a hole drift current $J_{hd}(W_A)$ from the depleted absorber at the interface W_A, the boundary condition at this location is modified to be $J(W_A) \approx J_{en}(W_A) + J_{hd}(W_A)$. Following the approximation in [28], the electron current $J_{en}(W_A)$ injected into the subsequent layer from this region is given by

$$J_{en}(W_A,\omega) = -qG_0W_A \cdot H_{\text{diff}}(\omega) \tag{5}$$

where $H_{\text{diff}}(\omega) \approx 1/(1+j\omega\tau_{\text{diff}})$ denotes the diffusion transfer function of the p-type layer, with $\tau_{\text{diff}} = W_A^2/(2D_e) + W_A/v_{\text{th}}$. v_{th} is the thermionic emission velocity [28]. By neglecting the dielectric relaxation effect within this layer, the total current is considered to be constant. Consequently, the total current density in this region is

$$\int_0^{W_A}(J_{en}+J_{hn})\,dx \approx W_A[J_{en}(W_A)+J_{hd}(W_A)] \tag{6}$$

In Region II, both electrons and holes are assumed to drift at their saturation velocities. The total current density in this region is given by

$$J_{ed}(x) + J_{hd}(x) = q(nv_e + pv_h) \tag{7}$$

By solving Equations (4c) and (4d), applying the boundary condition at W_A and coupling with (7), we can obtain

$$\begin{aligned} J_e(x) &= \frac{-qG_0}{j\omega/v_e - \alpha}\left[e^{-\alpha x} - e^{-\alpha W_A} e^{-j\omega\frac{x-W_A}{v_e}}\right] \\ J_h(x) &= \frac{-qG_0}{j\omega/v_h + \alpha}\left[e^{-\alpha x} - e^{-\alpha W_B} e^{-j\omega\frac{W_B-x}{v_h}}\right] \end{aligned} \tag{8}$$

In Region III, regarding electron drift current J_{ec} in the collection layer as the current induced in a parallel capacitor, it can be expressed as [27]

$$J_{ec}(\omega) = J_e(W_B) \cdot \frac{\sin(\omega\tau_c/2)}{(\omega\tau_c/2)\, e^{\frac{j\omega\tau_c}{2}}} \tag{9}$$

The injection current $J_e(W_B)$ is obtained by evaluating the Region II electron solution at $x = W_B$:

$$J_e(W_B) = J_{en}(W_A)e^{-j\omega\tau_{be}} + J_{ed}(W_B) \tag{10}$$

where $\tau_{be} = W_b/v_e$ is the electron transit time across Region II and $\tau_c = W_c/v_c$ is the transit time across the collection layer. $W_b(W_B - W_A)$ and W_c $(W - W_B)$ are the thicknesses of the depleted absorber and collector, respectively. Notably, v_c represents the overshoot velocity of electrons in InP to simulate overshoot phenomena under a certain electrical field [29].

By summarizing the aforementioned analysis and substituting the respective components into Equation (3), the analytical expression for the total photocurrent density is obtained as

$$\begin{aligned} J_{\text{tot}}(\omega) = \frac{W_A}{W}\left[J_{\text{en}}(W_A) - \frac{qG_0}{j\omega/v_h + \alpha}\left(e^{-\alpha W_A} - e^{-\alpha W_B} e^{-j\omega\tau_{bh}}\right)\right] + \frac{1}{W}\left\{J_{\text{en}}(W_A)\frac{1 - e^{-j\omega\tau_{be}}}{j\omega/v_e}\right. \\ - \frac{qG_0}{j\omega/v_e - \alpha}\left[\frac{e^{-\alpha W_A} - e^{-\alpha W_B}}{\alpha} - e^{-\alpha W_A}\frac{1 - e^{-j\omega\tau_{be}}}{j\omega/v_e}\right] \\ - \frac{qG_0}{j\omega/v_h + \alpha}\left[\frac{e^{-\alpha W_A} - e^{-\alpha W_B}}{\alpha} - e^{-\alpha W_A}\frac{1 - e^{-j\omega\tau_{be}}}{j\omega/v_e}\right] \\ \left. + W_c\left[\frac{\sin(\omega\tau_c/2)}{\omega\tau_c/2}e^{-j\omega\tau_c/2}\right] \times \left[J_{\text{en}}(W_A)e^{-j\omega\tau_{be}} - \frac{qG_0}{j\omega/v_e - \alpha}\left(e^{-\alpha W_B} - e^{-\alpha W_A}e^{-j\omega\tau_{be}}\right)\right]\right\} \end{aligned} \tag{11}$$

Figure 4 presents the intrinsic bandwidth of the MUTC-PD, calculated using the derived analytical expression (Equation (11)) and compared against numerical simulation results. $In_{0.53}Ga_{0.47}As$ is selected as the absorber material with a bandgap of approximately 0.74 eV during calculation. The key physical parameters are summarized in Table 1 [12,14,27,30]. In the analytical calculation, the electron velocity in the collector is set to the overshoot velocity (v_c) to account for non-stationary transport effects under high electric fields. To simplify the derivation, certain secondary effects such as carrier recombination and space charge accumulation are neglected. Additionally, the model assumes unity quantum efficiency within the absorber. Consequently, the overall simulated bandwidths (symbols with error bars) in Figure 4a fit the calculated analytical results closely, showing consistent peak positions and evolutionary trends. To further demonstrate the robustness of our theoretical framework, Figure 4b explicitly plots the detailed frequency response for the

specific structural configuration that exhibits the maximum bandwidth discrepancy. The slight deviation primarily stems from the simplified assumptions in the analytical model. Nevertheless, even in this worst case, the analytical curve and numerical simulation align remarkably well with a maximum error of less than 6%. This strong agreement conclusively validates the reliability and accuracy of the proposed AC small-signal analytical model as a highly efficient tool for optimizing the epitaxial structure.

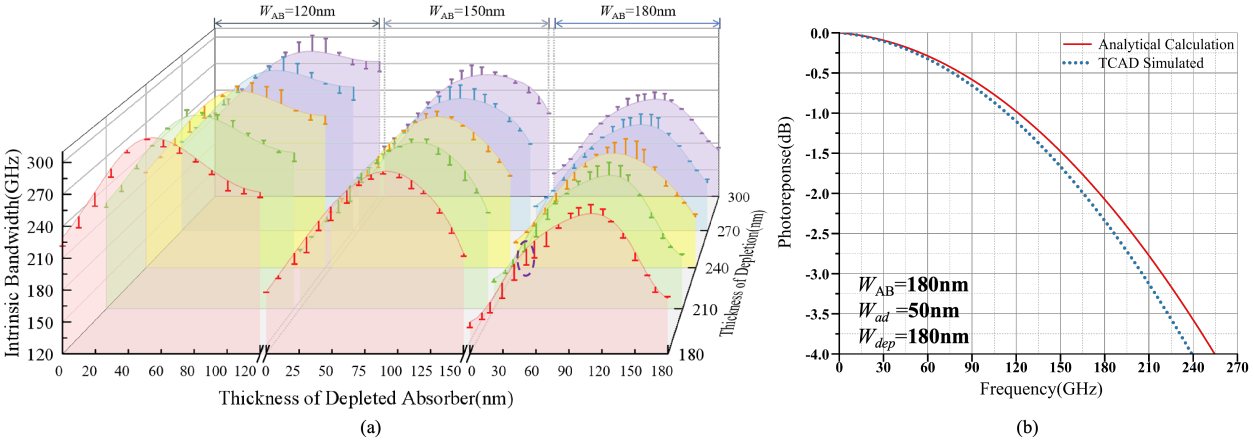


Figure 4. Comparison between analytical and numerical results: (**a**) Calculated (curves) and simulated (symbols with error bars) intrinsic bandwidth versus the thickness of the depleted absorber (W_{ad}) and depletion region (W_{dep}). (**b**) Detailed frequency response comparison between the analytical calculation and TCAD simulation for the configuration exhibiting the maximum discrepancy ($W_{\mathrm{AB}} = 180$ nm, $W_{ad} = 50$ nm, and $W_{dep} = 180$ nm).

Table 1. Parameters used for response calculation [12,14,27,30].

Parameter	Implication	Value
G_0	Optical generation rate	$1 \times 10^{35}\,\mathrm{m}^{-3}$
α	Absorption in $In_{0.53}Ga_{0.47}As$	$0.67 \times 10^{6}\,\mathrm{m}^{-1}$
v_h	Hole saturation velocity	5.0×10^{6} cm/s
v_e	Electron saturation velocity	6.5×10^{6} cm/s
v_c	Electron overshoot velocity in InP	3.5×10^{7} cm/s
v_{th}	Thermionic emission velocity in $In_{0.53}Ga_{0.47}As$	2.5×10^{7} cm/s
q	Electron charge	1.60×10^{-19} C
kT/q	Thermal voltage	0.026 V
μ_e	Electron mobility in p-Type $In_{0.53}Ga_{0.47}As$	$12,000\,\mathrm{cm}^2/(\mathrm{V}\cdot\mathrm{s})$
ϵ_0	Vacuum permittivity	8.854×10^{-14} F/cm
$\epsilon_{r,\mathrm{InP}}$	Relative permittivity of InP	$12.5\epsilon_0$
$\epsilon_{r,\mathrm{InGaAs}}$	Relative permittivity of $In_{0.53}Ga_{0.47}As$	$13.9\epsilon_0$

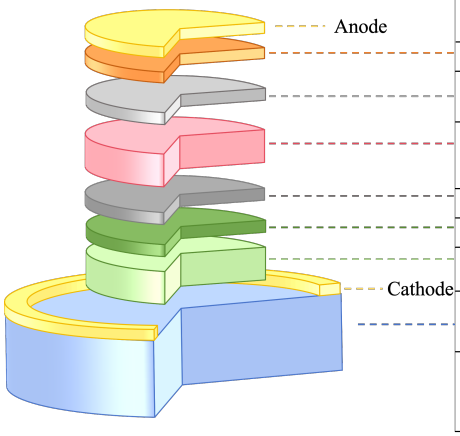
Based on the data from Figure 4, we present a comprehensive discussion structured around three dimensions: evolution within a single structure, lateral comparison of absorption layer thicknesses, and vertical comparison of depletion layer thicknesses. Under fixed total absorber ($W_{\mathrm{AB}} = W_{\mathrm{B}}$) and depletion ($W_{dep} = W - W_{\mathrm{A}}$) thicknesses, the intrinsic bandwidth exhibits a distinct rise-then-fall trend with increasing W_b, indicating a clear optimal operating point. The initial rise is driven by the reduction in the electron diffusion path in W_{A}. The subsequent fall is caused by the excessive transit time of slow holes in the thickened depleted absorber. Comparing the two endpoints, the bandwidth at the maximal depletion limit (DDR-PD-like) is consistently higher than at the minimal depletion limit (UTC-PD-like), which suggests that even relatively slow hole drift under a strong electric field is superior to long-distance electron diffusion. Fixing W_{dep}, we compare the three datasets where W_{AB} = 120, 150, and 180 nm laterally. The optimal operating point shifts to the right as W_{AB} increases, implying a larger optimal W_b. As W_b increases, the penalty from

electron diffusion time grows quadratically ($\tau_{\text{diff}} \propto W_{\text{A}}^2$). To counteract this, the device must prioritize suppressing the diffusion tail by increasing the depleted fraction W_b/W_{AB}, even at the cost of linearly increasing the hole transit time. Fixing W_{AB}, the overall bandwidth universally decreases as W_{dep} increases with the position of the bandwidth peak remaining virtually unchanged. This behavior indicates that the optimization of the layer structure is primarily governed by the internal carrier transport dynamics within the absorber. The optimal W_b is determined by the trade-off between electron diffusion in the non-depleted absorber and hole drift in the depleted absorber—a balance strictly constrained by W_{AB}. The collector layer acts predominantly as a drift region, whose thickness increase introduces an additional transit delay that suppresses the overall speed but essentially decouples from the local diffusion–drift optimization within the absorber.

While the analytical model provides a robust theoretical framework under low-power conditions, high-speed photodetectors in practical communication systems often operate under high optical power densities where nonlinear effects arise. Therefore, the subsequent section employs the commercial simulator Silvaco Atlas to investigate the device performance under high-injection conditions, explicitly considering space charge effects and carrier concentration dynamics.

3. Detailed MUTC-PD Structure

Figure 5 illustrates the schematic diagram and the epitaxial layer structure of the designed bottom-illuminated MUTC-PD operating at 1550 nm. Based on the theoretical optimization analysis above, with the total absorber thickness fixed at 120 nm and the depletion width at 240 nm, the optimal configuration is identified as a 70 nm p-doped non-depleted absorber, a 50 nm depleted absorber, and a 170 nm collector. This optimized structure yields a theoretical intrinsic bandwidth of 303.45 GHz.



Layer	Material	Thickness (nm)	Doping (cm-3)	Bandgap (eV)
P contact	$In_{0.53}Ga_{0.47}As$	40	p:>2×10^{19}	0.74
Difussion block	$In_{0.6}Ga_{0.4}As_{0.85}P_{0.15}$	20	p:2×10^{19}	0.805
Absorber	$In_{0.53}Ga_{0.47}As$	70	p:2×10^{18}	0.74
	$In_{0.53}Ga_{0.47}As$	50	n:2×10^{16}	
Spacer	InGaAsP	10	i	0.74~1.34
Cliff	InP	10	n:2×10^{18}	1.34
Collector	InP	170	n:2×10^{16}	
N contact	InP	200	n:>2×10^{19}	
S.I InP Sub				

Figure 5. Cross-sectional schematic and detailed epitaxial layer structure of the optimized MUTC-PD.

The epitaxial layers were grown on a semi-insulating InP substrate, beginning with a 40 nm heavily p-doped $In_{0.53}Ga_{0.47}As$ contact layer, followed by a 20 nm p-type InGaAsP (Q1.4) electron-blocking layer to suppress electron diffusion into the contact. $In_{0.53}Ga_{0.47}As$ is selected as the 120 nm absorber material because it is perfectly lattice-matched to the InP substrate, which ensures high epitaxial crystalline quality and low defect density. Simultaneously, this specific narrow bandgap guarantees highly efficient absorption of the 1550 nm incident light. A 170 nm lightly n-doped InP layer is adopted as the collector. To smooth band discontinuities and optimize the internal electric field profile, a 10 nm InGaAsP transition layer and a 10 nm heavily n-doped InP cliff layer are inserted at the

absorber/collector interface. The structure concludes with a 200 nm heavily n-doped InP contact layer. The anode and cathode electrodes are deposited on the p-type and n-type contact layers, respectively.

The overall 3-dB bandwidth (f_{3dB}) is determined by the interplay of the intrinsic bandwidth ($f_{intrinsic}$) and the RC-limited bandwidth (f_{RC}), governed by the relationship

$$\frac{1}{f_{3dB}^2} = \frac{1}{f_{intrinsic}^2} + \frac{1}{f_{RC}^2} \tag{12}$$

The RC-limited bandwidth is defined as

$$f_{RC} = \frac{1}{2\pi RC} \tag{13}$$

where R represents the sum of load resistance R_L and series resistance R_S. C denotes the junction capacitance given by $C = \varepsilon A/W_{dep}$, where A is the junction area and ε is the relative permittivities of depletion. To enhance high-speed performance, coplanar lines with an equivalent impedance of 12.5Ω are typically utilized to minimize the load resistance [28].

A critical design trade-off exists regarding the junction area and depletion thickness. Although a larger area benefits saturation performance and coupling efficiency, and a thinner depletion region improves $f_{intrinsic}$ by shortening transit time, both a large area and a thin depletion region result in increased junction capacitance and decreased f_{RC}. To ensure the device bandwidth is primarily limited by carrier transport rather than parasitic effects, a device diameter of 5 μm was selected. With the depletion region thickness, series resistance and parasitic capacitance set to 240 nm, 4Ω and 4 fF, respectively [10,14], the calculated f_{RC} exceeds 700 GHz. As this value is significantly higher than the theoretical intrinsic bandwidth derived in Section 2, the subsequent optimization analysis focuses exclusively on the intrinsic transport characteristics of the designed MUTC-PD.

4. Simulation Results with Varied Input Optical Power

In this section, we investigate the high-speed performance of the optimized MUTC-PD structure in Section 3 under high optical incident intensity using the commercial simulator Silvaco Atlas based on numerical methods. Key parameters including intrinsic bandwidth, carrier concentration, and electric field magnitude are investigated under high-incident-optical-intensity conditions. The device operates under a reverse bias of −3.5 V to ensure complete depletion of the depletion region.

The incident optical intensity is swept from 1×10^4 W/cm^2 to 3×10^5 W/cm^2. Figure 6a illustrates the dependence of frequency response on optical intensity, while Figure 6b depicts the trend in $f_{intrinsic}$, which peaks at 325.82 GHz at 7×10^4 W/cm^2 and then sharply declines to 182.26 GHz at 3×10^5 W/cm^2. The phenomenon arises from two competing carrier transport mechanisms. We further provide the distribution of the internal electric field and electron concentration of the device under different incident optical power densities in Figure 7. At lower intensities (<7×10^4 W/cm^2), photogenerated holes are rapidly swept in the heavily p-doped absorber, establishing a substantial hole current. According to charge continuity, the hole current induces a self-consistent quasielectric field in the absorber, thereby enhancing electron drift velocity toward the collector. This drift-enhancement effect effectively suppresses the slow diffusion component, reducing electron transit time and thereby boosting bandwidth beyond its small-signal prediction.

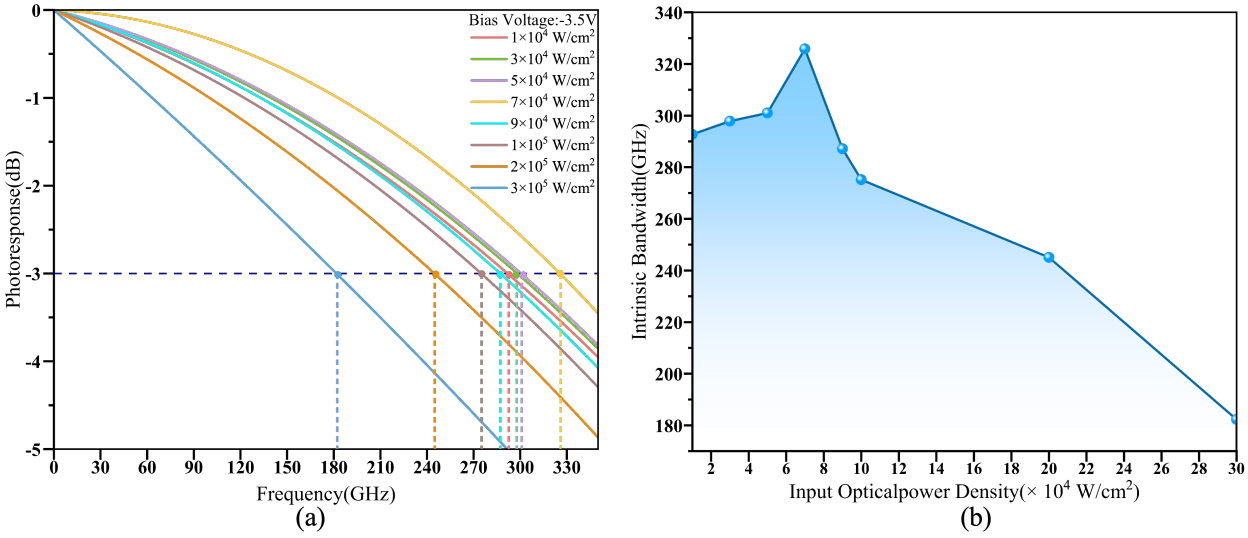


Figure 6. Simulation results: (**a**) frequency response and (**b**) intrinsic bandwidth evolution under varying incident optical intensities at −3.5 V bias.

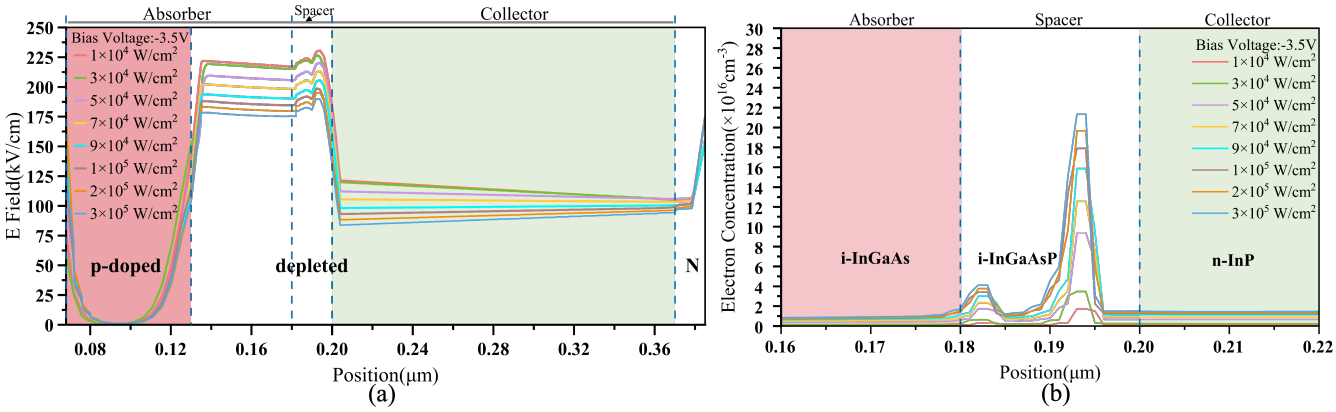


Figure 7. (**a**) Internal electric field distribution along the position; (**b**) electron concentration in depletion.

Beyond the optimal intensity of 7×10^4 W/cm^2 at −3.5 V DC bias, the bandwidth begins to degrade due to carrier accumulation-induced space charge effects. This phenomenon occurs when excessive photogenerated carriers accumulate near the heterointerface between the depleted absorber and collector. The resulting localized negative space charge perturbs the internal electric field profile via Poisson's equation, causing a significant reduction in the electric field strength within the depleted absorber. While electron velocity in the collector remains largely unaffected due to saturation, the weakened field severely impedes the drift of holes in the depleted absorber. As a result, the hole transit time becomes the dominant factor limiting the frequency response, leading to the observed bandwidth compression.

Therefore, the bandwidth underscores that the linear dynamic range of the high-speed MUTC-PD should be defined not merely by DC photocurrent saturation, but more fundamentally by the stability of the intrinsic bandwidth under high injection.

5. Conclusions

In this work, we developed a hybrid analytical–numerical design method for a high-speed MUTC-PD operating at high incident optical intensity. An analytical model based on

1D carrier continuity and Poisson equations enabled rapid structural optimization, yielding a predicted small-signal bandwidth of 303.45 GHz.

Through substantial simulations, we uncovered a bandwidth-enhancing regime at moderate optical powers (peaking at 325.82 GHz), driven by a self-induced drift field. Conversely, we identified internal field collapse due to space charge effects as the fundamental bottleneck at high injection.

Our results establish bandwidth stability under high optical intensity as a key figure of merit for linear high-speed photodetection. The proposed methodology offers a physically transparent and efficient pathway for co-optimizing speed and linearity in next-generation photodetectors for applications such as coherent communications, microwave photonics and solid-state LiDAR.

Author Contributions: Conceptualization, X.Z.; Methodology, X.Z.; Software, X.Z.; Validation, X.Z.; Formal analysis, X.Z.; Data curation, X.Z.; Writing—original draft, X.Z.; Writing—review & editing, X.D.; Supervision, X.D.; Funding acquisition, X.D. All authors have read and agreed to the published version of the manuscript.

Funding: This document is the result of the research project funded by the National Natural Science Foundation of China under Grant 62474023.

Data Availability Statement: Data are contained within the article.

Conflicts of Interest: The authors declare no conflicts of interest. The funders had no role in the design of the study; in the collection, analyses, or interpretation of data; in the writing of the manuscript; or in the decision to publish the results.

References

1. Dong, X.; Liu, K. Modified uni-traveling-carrier photodetector with its optimized cliff layer. *Sensors* **2024**, *24*, 2020. [CrossRef] [PubMed]
2. Sun, X. Review of Photodetectors for Space Lidars. *Sensors* **2024**, *24*, 6620. [CrossRef] [PubMed]
3. Qu, H.; Wang, W.; Chen, B.; Li, X.; Li, Y.; Hu, H.; Li, J.; Wang, Z.; Zhi, Z.; Liu, X.; et al. Novel three-electrode Ge/Si balanced avalanche photodetector for FMCW LiDAR application. *Photonics Res.* **2024**, *13*, 2803–2812. [CrossRef]
4. Kato, K. Ultrawide-band/high-frequency photodetectors. *IEEE Trans. Microw. Theory Technol.* **1999**, *47*, 1265–1281. [CrossRef]
5. Gärtner, W.W. Depletion-layer photoeffects in semiconductors. *Phys. Rev.* **1959**, *116*, 84–87. [CrossRef]
6. Lucovsky, G.; Schwarz, R.F.; Emmons, R.B. Transit-time considerations in p-i-n diodes. *J. Appl. Phys.* **1964**, *35*, 622–628. [CrossRef]
7. Effenberger, F.J.; Joshi, A.M. Ultrafast, dual-depletion region, InGaAs/InP p-i-n detector. *J. Light. Technol.* **1996**, *14*, 1859–1864. [CrossRef]
8. Yuan, W.; Duan, X.; Ren, R.; Li, K.; Li, Y.; Liu, K.; Huang, Y.; Ren, X. Modified dual-depletion region photodetector. In Proceedings of the 2022 Asia Communications and Photonics Conference (ACP), Shenzhen, China, 5–8 November 2022; pp. 1500–1503.
9. Ishibashi, T.; Shimizu, N.; Kodama, S.; Ito, H.; Nagatsuma, T.; Furuta, T. Uni-traveling-carrier photodiodes. In *Ultrafast Electronics and Optoelectronics*; Optica Publishing Group: Washington, DC, USA, 1997; p. UC3.
10. Xiong, W.; Peng, Z.; Yao, R.; Guo, Q.; Chi, C.; Ji, C. Systematic analysis of a modified uni-traveling-carrier photodiode under high-power operating conditions. *Photonics* **2023**, *10*, 474. [CrossRef]
11. Jun, D.-H.; Jang, J.-H.; Lee, D.-S.; Lee, D.-H.; Park, H.-M.; Choi, J.-H.; Park, C.-S.; Kang, S.-S.; Kim, J.-H.; Lee, E.-H.; et al. Improved efficiency-bandwidth product of modified uni-traveling carrier photodiode structures using an undoped photo-absorption layer. *Jpn. J. Appl. Phys.* **2006**, *45*, 3475. [CrossRef]
12. Dong, X.; Liu, K.; Huang, Y.; Duan, X.; Wang, Q.; Ren, X. Design of high-speed UTC-PD with optimization of its electron transit performance and parasitic capacitance. *IEEE Photonics J.* **2023**, *15*, 9. [CrossRef]
13. Li, L.; Long, T.; Yang, X.; Zhang, Z.; Wang, L.; Wang, J.; Wang, M.; Lu, J.; Yu, J.; Chen, B. Modified uni-travelling-carrier photodiodes with 206 GHz bandwidth and 0.81 A W^{-1} external responsivity. *Nat. Photonics* **2025**, *19*, 1301–1308. [CrossRef]
14. Tian, Y.; Xiong, B.; Sun, C.; Hao, Z.; Wang, J.; Wang, L.; Han, Y.; Li, H.; Gan, L.; Luo, Y. Ultrafast MUTC photodiodes over 200 GHz with high saturation power. *Opt. Express* **2023**, *31*, 23792–23802. [CrossRef]
15. Nawaz, M.Z.; Bilal, M.; Ali, I.; Ahmed, I.; Hassan, M.; Abbas, F. Tuning Performance of Heterojunction Flexible Photodetectors by Energy Band Alignment Engineering. *ACS Appl. Nano Mater.* **2024**, *7*, 15354–15364. [CrossRef]

16. Nawaz, M.Z.; Khaleeq, A.; Illarionov, Y. Flexible Self-Powered $Ti_3C_2T_x$MXene Nanosheet/CdS Nanobelt Photodetector with Enhanced Responsivity and Photosensitivity. *ACS Appl. Nano Mater.* **2025**, *8*, 11015–11025. [CrossRef]
17. Nawaz, M.Z.; Ahmad, W.; Chen, Q.; Cao, S.; Zhang, H.; Liu, Y.; Yang, H.; Zhao, L. Broadband and low-light photodetection in a flexible 2D $Ti_3C_2T_x$ MXene/1D-SbSI nanowire heterojunction photodetector. *Mater. Res. Bull.* **2026**, *193*, 113648. [CrossRef]
18. Zhang, J.; Nawaz, M.Z.; Zhou, X.; Xu, L.; Wu, J.; Wang, C. $V_3O_7{\cdot}H_2O$ Nanowire Film/T_d-$MoTe_2$ Flake Mixed-dimensional Van der Waals Heterostructure for Photodetection. *Chem. Lett.* **2023**, *52*, 365–369. [CrossRef]
19. Sun, X.; Ye, S.; Seddon, J.; Renaud, C.C.; Hou, L.; Marsh, J.H. Modeling and Measurement of a HSQ Passivated UTC-PD with a 68.9 GHz Bandwidth. In Proceedings of the 2021 IEEE Photonics Conference (IPC 2021), Vancouver, BC, Canada, 18–21 October 2021; pp. 1–2.
20. Li, Q.; Li, K.; Fu, Y.; Xie, X.; Yang, Z.; Beling, A.; Campbell, J.C. High-power flip-chip bonded photodiode with 110 GHz bandwidth. *J. Light. Technol.* **2016**, 34, 2139–2144. [CrossRef]
21. Marlow, G.S.; Das, M.B. The effects of contact size and non-zero metal resistance on the determination of specific contact resistance. *Solid-State Electron.* **1982**, 25, 91–94. [CrossRef]
22. Capmany, J.; Novak, D. Microwave photonics combines two worlds. *Nat. Photonics* **2007**, 1, 319–330. [CrossRef]
23. Ishibashi, T. Uni-traveling-carrier photodiodes. *J. Appl. Phys.* **2020**, *127*, 031101. [CrossRef]
24. Mukherjee, C.; Guendouz, D.; Deng, M.; Bertin, H.; Bobin, A.; Vaissiere, N.; Caillaud, C.; Arabhavi, A.M.; Chaudhary, R.; Ostinelli, O.; et al. SPICE Modeling in Verilog-A for Photo-Response in UTC-Photodiodes Targeting Beyond-5G Circuit Design. *IEEE Trans. Comput.-Aided Des. Integr. Circuits Syst.* **2023**, *42*, 3045–3052. [CrossRef]
25. Ishibashi, T.; Muramoto, Y.; Yoshimatsu, T.; Ito, H. Unitraveling-carrier photodiodes for terahertz applications. *IEEE J. Sel. Top. Quantum Electron.* **2014**, *20*, 79–88. [CrossRef]
26. Ghione, G. *Semiconductor Devices for High-Speed Optoelectronics*; Cambridge University Press: Cambridge, UK, 2009; pp. 159–211.
27. Ishibashi, T.; Kodama, S.; Shimizu, N.; Furuta, T. High-Speed Response of Uni-Traveling-Carrier Photodiodes. *Jpn. J. Appl. Phys.* **1997**, *36*, 6263. [CrossRef]
28. Ishibashi, T.; Furuta, T.; Fushimi, H.; Kodama, S.; Ito, H.; Nagatsuma, T.; Shimizu, N.; Miyamoto, Y. InP/InGaAs uni-traveling-carrier photodiodes. *IEICE Trans. Electron.* **2000**, *83*, 938–949.
29. Maloney, T.J.; Frey, J. Transient and steady-state electron transport properties of GaAs and InP. *J. Appl. Phys.* **1977**, *48*, 781–787. [CrossRef]
30. Tan, S.H.; Wang, X.J.; Huang, Y.Q.; Liu, K.; Duan, X.F.; Ren, X.M. A high-speed and high-power modified uni-traveling carrier photodiode at 1310nm wavelength. *J. Optoelectron. Laser* **2025**, 36, 561–567.

Disclaimer/Publisher's Note: The statements, opinions and data contained in all publications are solely those of the individual author(s) and contributor(s) and not of MDPI and/or the editor(s). MDPI and/or the editor(s) disclaim responsibility for any injury to people or property resulting from any ideas, methods, instructions or products referred to in the content.